Received: 17 December 2025 | Revised: 17 March 2026 | Accepted: 10 April 2026 | Published online: 11 May 2026

RESEARCH ARTICLE

Archives of Advanced Engineering Science
2026, Vol. 4(4) 390–401
DOI: 10.47852/bonviewAAES62028822

Crystallization of Tin in Iron–Carbon Alloys

Sergey Vasilyevich Davydov[1,*]

[1] *Bryansk State Technical University, Russia*

Abstract: In this work, a set of experimental studies has been performed using the example of high-strength cast iron microalloyed with 0.05–0.06% Sn. The Sn content in the studied intermetallides varies in a fairly wide range: from 1.5% to 16.0%. From the standpoint of alloy theory, tin intermetallides with their variable composition are solid homogeneous solutions based on FeSn. It was found that the average tin content in ferrite pearlite of cast iron structure varies significantly: 0.06–0.81% Sn and in some zones up to 1.5% Sn. Consequently, pearlite ferrite in the cast structure of high-strength cast iron is a super-supersaturated (compared with the equilibrium composition according to the Fe–Sn diagram) solid solution of tin in the α-Fe polymorph (ferrite). The degree of dispersion of high-strength cast iron pearlite was determined both after its microalloying with tin in the amount of Sn = 0.05–0.06%, and without alloying. The average degree of dispersion of pearlite in both cast irons turned out to be almost the same. In cast iron with tin, Δ_{Sn} = 0.13 microns, while in cast iron without tin, Δ_0 = 0.14 microns; that is, the degree of dispersion of pearlite does not depend on its alloying with tin within these limits.

Keywords: tin intermetallics, steel, cast iron, pearlite

1. Introduction

Based on the analysis of available data [1–7], it was established that tin as an alloying element is actively used both in special cast irons [1–5] and in steels [6, 7]. Alloying steels with tin is used to improve their machinability as a substitute for environmentally hazardous elements such as selenium, tellurium, and bismuth. Tin is also used in ferritic and austenitic-martensitic steels to improve corrosion resistance and as a component of corrosion-resistant surface coatings on steel products. International standards such as ASTM A623, ISO 11949, JIS G 3302, and others regulate the use of tin in steel.

While tin is used in limited quantities and strictly functionally in steels, it is used in special cast irons (high-strength and compacted graphite) in fairly large quantities to achieve a range of performance properties.

Tin is one of the most effective, yet scarce and expensive, microalloying agents, not a carbide-forming, effective pearlitizing agent for the metallic matrix of cast iron. Its general mechanism of influence on cast iron structure formation is associated with a decrease in the rate of carbon diffusion in austenite, stabilization of eutectoid cementite, and a sharp reduction in ferrite content. The addition of tin in quantities of approximately 0.10–0.15% appears to be the only practical way to prevent ferrite growth in a stable eutectoid reaction and the complete transformation of the material matrix into pearlite in a metastable eutectoid system [1–5].

It has been shown [1–5] that tin contents above 0.05% lead to a decrease in impact toughness and ductility, an increase in hardness, and, overall, embrittlement of high-strength cast iron. At the same time, its lower content does not allow to fully achieve the strengthening effect and pearlitization of the metal base; therefore, it is necessary to study the effect on the microstructure and mechanical properties of the boundary range of tin content in high-strength cast iron of at least 0.05–0.06%. At the same time, pearlitization of the matrix, a decrease in the proportion of ferrite, and an increase in the degree of pearlite dispersion improve the wear-resistant properties of cast iron with a vermicular form of graphite when it is micro alloyed with tin at 0.092% [4]. However, alloying with Sn (from 0.010 to 0.118%) causes more brittle fractures in gray cast irons with a lamellar form of graphite compared to the unalloyed state [5].

The accumulation of tin in scrap metal and its conversion to steel or cast iron is currently an intractable problem, as slag and flotation methods are virtually impossible to extract from iron–carbon melts in significant quantities. The most actively studied technology for evaporating Sn from liquid iron is electromagnetic levitation melting at 1600 °C [8], as well as conventional metallurgical processes [9], for processing and refining ferrous scrap.

In this paper, the crystallization processes and distribution of tin within the phases of cast iron are examined using tin microalloying of ductile iron as an example.

The aim of the research is to evaluate the distribution of tin in ferrite pearlite plates, determine the degree of dispersion of pearlite in high-strength cast iron both after its microalloying with tin in the amount of Sn = 0.05–0.06% and without alloying, and also study the conditions for the formation of a barrier layer of intermetallic compounds along the interphase boundaries of the structural components of the alloy.

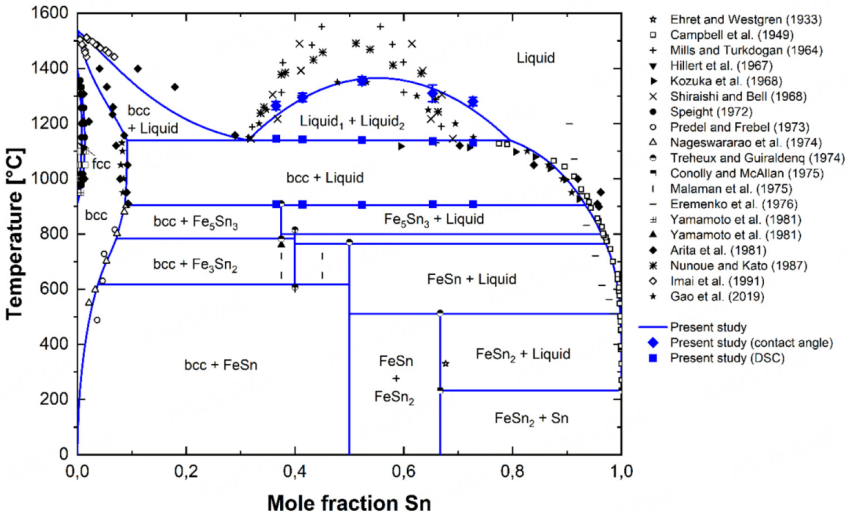
2. Current State of Research in the Fe–Sn System

Due to the increasing negative impact of accumulated tin in "contaminated" cast irons and steels, various studies are currently

***Corresponding author:** Sergey Vasilyevich Davydov, Bryansk State Technical University, Russia. Email: davidov69@tu-bryansk.ru; fulleren_grafen@mail.ru

© The Author(s) 2026. Published by BON VIEW PUBLISHING PTE. LTD. This is an open access article under the CC BY License (https://creativecommons.org/licenses/by/4.0/).

Figure 1
An updated diagram of the state of alloys of the Fe–Sn system

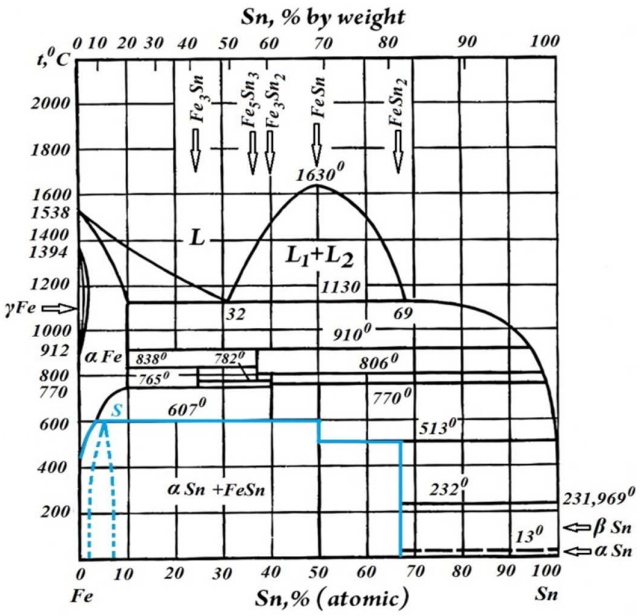


underway to assess the influence of tin on phase and structural transformations in the Fe–C system during alloy crystallization, as well as its effect on their mechanical and performance properties. In Park et al. [10], using significant experimental data from 1933 to 2019, the phase diagram profile of alloys in the Fe–Sn system was refined and calculated (Figure 1 [10]), and the specific features of certain phase transformations were identified.

The phase and structural composition of the Fe–Sn system were also studied based on experimental data on micro alloying of the Fe–C–Sn system to assess the effect of tin on phase equilibrium in this system with calculation of phase transformation temperatures in the solid state [11–13]. The thermodynamic and topological properties of the main phases in the Fe–Sn system were investigated based on a combination of experimental data, thermodynamic calculations, and calorimetric experiments [14]. The metastable Fe_3Sn phase was introduced into the Fe–Sn diagram for the first time, and the arrangement of the Fe_5Sn_3 and Fe_3Sn_2 phases was corrected in accordance with the measured and corrected temperature ranges. Figure 2 [15] shows the phase diagram of the Fe–Sn system alloys according to Lyakishev [15]. Figure 3 [15] shows an enlarged loop of solid solutions of tin in the γ-Fe and α-Fe polymorphs [15]. In the Fe–Sn system alloys, there are five intermetallic compounds: Fe_3Sn, Fe_5Sn_3, Fe_3Sn_2, FeSn, and $FeSn_2$. The first of these compounds is formed by a peritectoid reaction at 838 °C, while the others form by peritectic reactions at 910, 806, 770, and 513 °C, respectively (Figure 2 [15]). The two-phase regions of the phase diagram consist of a solid solution of Sn in α-Fe (α-Fe(Sn)), and the corresponding intermetallic compounds (Figure 2) [15]. In the temperature range t = 0…607 °C, it is the intermetallic compound FeSn (Figure 2 [15], the region is highlighted by the blue line); in the range t = 607…765 °C, it is Fe_3Sn_2; in the range t = 765…838 °C, it is Fe_3Sn; and in the range t = 838…910 °C, it is Fe_5Sn_3. A distinctive element of the Fe–Sn diagram is the loop of solid solutions of tin in the γ-Fe and α-Fe polymorphs (Figure 3 [15]).

The extreme points of the loop at 1100 °C have the following coordinates (Figure 3 [15]): 1.5% mass. Sn (0.71% at. Sn) is the minimum degree of Sn solubility in the γ-Fe polymorph and 2.7% mass. Sn (1.29% at. Sn) is the maximum solubility of Sn in the α-Fe polymorph [16].

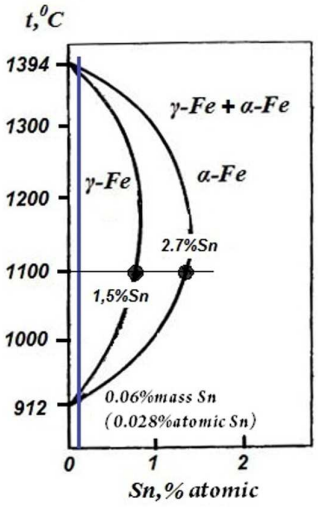
Figure 2
Diagrams of the state of alloys in the Fe–Sn system according to N.P. Lyakishev; the dashed line shows the expected homogeneity region of the FeSn-based solid solution



The limiting solubility of Sn in the α-Fe polymorph upon cooling is constant in the range of 1130–765 °C (Figure 2 [15]) and is 20.0% by weight Sn (10.0% at. Sn) and subsequently decreases to zero below 200 °C (Figure 1 [10]). At a temperature of 607 °C (Figure 2 [15]), the solubility of Sn is 6.57% by weight (3.2% at. Sn) [17].

Using the Fe–Sn diagram (Figures 1–3) [10, 15], we can, in a preliminary analysis, investigate the embrittlement mechanism and generally evaluate the influence of tin on phase and structural transformations in iron–carbon alloys. The tin content studied in this article, in the range of 0.02–0.15%, allows us to draw a clear conclusion: the intermetallic compound FeSn plays a key role in

Figure 3
A loop of solid tin solutions in γ-Fe and α-Fe polymorphs; the blue line conditionally corresponds to the maximum tin content in experimental melts of 0.06 mm mass Sn



the crystallization structure of iron–carbon alloys, precipitating in the two-phase region α-Fe + FeSn, outlined by the blue line in Figure 2 [15].

As an analysis of a number of modern studies [3–14] shows, tin has little effect on the carbon content of the alloy [12]; therefore, its influence is valid for both steels and cast irons with different graphite forms.

3. Crystallization Processes of Tin Intermetallic Compounds

Let us consider the crystallization process of the intermetallic compound FeSn in the diagram (Figure 4) as applied to the solidification of austenite along the ES line (see the Fe–C diagram). Crystallization of structural cast irons is completed after the eutectic decomposition of the liquid at t = 1147 °C. At this temperature, the maximum concentration of Sn in austenite is t. E (see Fe–C diagram) can be 1.5% Sn (Figure 2 [15]), which is incomparable with the range of tin concentrations considered in this review.

In the temperature range of 1147–912 °C (Figure 4(a)), carbon diffusion will begin in austenite along the ES line (see the Fe–C diagram) (red arrows, Figure 4(a)), with the release of cementite CII precipitation along the austenite grain interfaces (cementite precipitation is not shown).

In the temperature range of 912–723 °C (Figure 4(b)), with decreasing temperature, the solubility of Sn in austenite γ-Fe begins to decrease (Figure 2 [15]), and Sn diffusion to the austenite grain interface (Ay–Ay) will form a thin atomic layer supersaturated with Sn, which will block carbon diffusion (Ay→CII), "preserving" the supersaturation of the austenite grain with carbon (Csupersaturated) above its equilibrium concentration (Cbalanced) according to the Fe–C diagram. At a temperature of 912 °C of the α-Fe γ-Fe polymorphic transformation, the Sn concentration in austenite tends to zero (Figure 2 [15]). The Sn concentration in the atomic layer (Figure 4(b)) along the Ay–Ay interphase boundary will reach maximum supersaturation without the formation of the FeSn intermetallic compound, the crystallization of which will begin only when the cast iron is cooled below 200 °C (Figure 1 [10]).

According to Peng et al. [18], it was found that when quenching 20CrMnTi steel, containing 0.049% by weight of Sn, from 950 °C, the average Sn content at the boundaries and inside the austenite grains is 0.108% by weight and 0.045% by weight, respectively; that is, the Sn concentration at the interphase surface of the austenite grains exceeds the concentration inside the austenite grain by almost 2.5 times.

At a temperature of 723 °C (Figure 4(c)), due to carbon supersaturation in each austenite grain above the equilibrium concentration of Csupersaturated (Figure 4(b)) and the blocking of carbon diffusion by a highly concentrated atomic layer of Sn along the grain boundaries, austenite undergoes a eutectoid reaction, almost entirely transforming into pearlite (Figure 4(c)). This results in significant dispersion of pearlite colonies (additional hardness increase), and it can be assumed that Sn has a catalytic effect on their nucleation process. The resulting ferrite dissolves the residual tin content of the austenite; therefore, pearlite ferrite is a solid solution of tin in the α-Fe polymorph (Figure 2 [15]).

In the temperature range of 723–400 °C (Figure 4(c)), no phase transformations occur after pearlitization of the cast iron structure. Upon cooling the cast iron to a temperature of ~200 °C, the intermetallic compound FeSn will begin to precipitate in the system (Figure 1 [10]): intensely along the interphase surface of former austenite grains (Figure 4(d)) and less intensely along the F–C interphase surface in pearlite colonies due to the decomposition of the Sn solid solution in the α-Fe polymorph (not shown in the diagram in Figure 4).

Figure 4
Scheme of the crystallization process of Fe Sn intermetallic compound in high-strength cast iron (explanation in the text)

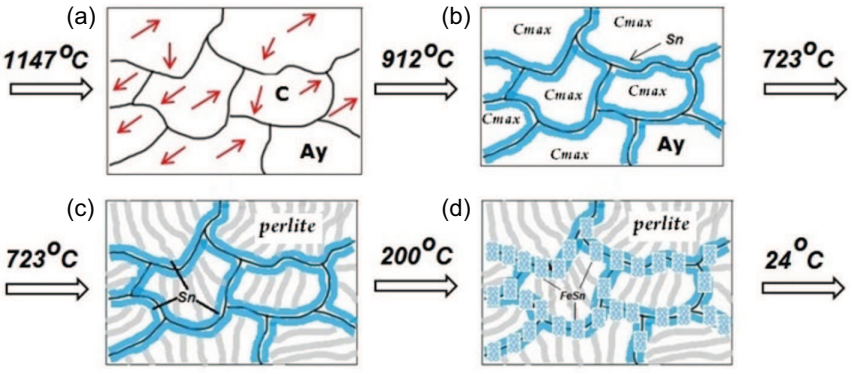
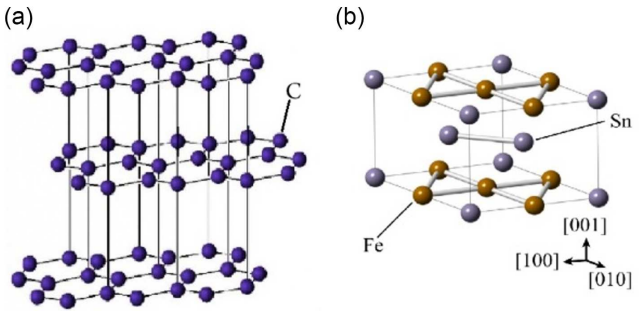


Figure 5
Crystal lattices of (a) graphite and (b) the intermetallic compound FeSn



The precipitation of the intermetallic compound FeSn in different structures results in two effects: dispersion strengthening of pearlite and embrittlement softening of the interphase surfaces of former austenite grains.

The crystal lattice of the intermetallic compound FeSn is identical to the crystal lattice of graphite. Graphite belongs to the hexagonal syngony, space group P63/mmc, with cell parameters a = 0.246 nm and c = 0.6708 nm (Figure 5(a)). The intermetallic compound FeSn or iron stannide also forms crystals of the hexagonal syngony, with space group P6/mmm and cell parameters a = 0.5298 nm and c = 0.4446 nm (Figure 5(b)).

In fact, the intermetallic compound FeSn, like graphite, has a layered structure (Figure 5(b)), between the layers of which a van der Waals bond or π-bond arises and within the layer between the tin atoms—a covalent bond [19]. The van der Waals bond is the most universal; it arises between any particles, but it is also the weakest bond—its energy is approximately two orders of magnitude lower than the energy of ionic and covalent bonds. In other words, the interphase surface is "covered" with a brittle intermetallic film, the structure of which is similar to the structure of brittle graphite, which is primarily destroyed by external influences. Accordiing to Sun and Tao [20], it was shown that Sn is released along the boundaries of austenite grains, embrittlement them, in the temperature range from 400 to 6000 °C.

According to Ribeiro et al. [21], the effect of varying silicon, copper, and tin concentrations on the microstructure and mechanical properties of compact graphite cast iron (CGA) for the manufacture of cylinder blocks and cylinder heads for diesel engines was investigated. Figure 6 [21] shows the microstructure of CGA cast iron with varying Sn contents. It was found that alloying with tin reduces the temperature ranges in which austenite and ferrite coexist.

Thus, the time interval for carbon diffusion during solidification is reduced, which helps suppress ferrite growth and increase pearlite dispersion, that is, decrease the distance between ferrite and cementite platelets in pearlite. Sn has barrier-forming properties that impede carbon diffusion. The addition of tin reduces ductility and degrades the fatigue resistance of cast iron.

Comparing the pearlitizing properties of copper and tin, it was found that the pearlitizing capacity of tin is approximately 10 times higher than that of copper. In Peng et al.'s study [18], the structural state of austenite was investigated during quenching from 950 °C of 20CrMnTi steel containing 0.004% by weight, 0.021% by weight, and 0.049% by weight Sn (Figure 7 [18]).

Intense Sn precipitation was observed, with the average Sn content at the austenite grain boundaries and within the grains amounting to 0.108% by weight and 0.045% by weight, respectively. This means that the Sn concentration at the austenite grain interface exceeds the Sn concentration within the austenite grain by almost 2.5 times. Tin precipitation along the austenite grain interface is the primary factor in steel embrittlement. The tin film is essentially a supersaturated solid solution of tin in the α-Fe polymorph (Figure 2 [15]). Another equally important factor that dramatically reduces steel ductility is the precipitation of a virtually continuous proeutectoid ferrite film at 750 °C along the austenite grain boundary in the fracture zones of the specimens (Figure 8 [18]).

The yield strength of ferrite is relatively low compared to that of austenite. This easily leads to stress concentration on the ferrite film, leading to reduced ductility and embrittlement of the metal base.

The formation of a continuous ferrite film along austenite grain boundaries is explained based on the Fe–Sn diagram (Figure 2 [15]) and the precipitation of tin along austenite grain boundaries (Figure 7 [18]). When the solubility of Sn in the solid solution of the α-Fe polymorph (Figure 7 [18]) decreases to practically zero (Figure 2 [15]), Sn, diffusing from the volumes of the films to their outer boundaries, will be released in the form of intermetallic compounds Fe3Sn or FeSn, depending on the level of supersaturation of the solid solution. In this case, the matrix of the solid solution is transformed into a ferrite film (Figure 8 [18]). Unfortunately, in Peng at al. [18], the structure of the ferrite film was not investigated for the detection of intermetallic compounds FeSn and Fe3Sn, precipitating along its boundaries. It can be assumed that the inclusions of intermetallic compounds will have a nanoscale dispersion.

It is virtually impossible to destroy precipitated intermetallic compounds by heat treatment, as they are thermally stable and do not decompose. For example, the intermetallic compound FeSn is thermally stable up to 700 °C [22]. At higher heating temperatures, Sn will transform into a solid solution (Figure 3 [15]).

Figure 6
Microstructure of cast iron with a compact graphite shape at different Sn contents: Sn 0.075%; 0.091% and 0.105%: A – pearlite; B – ferrite; C – graphite

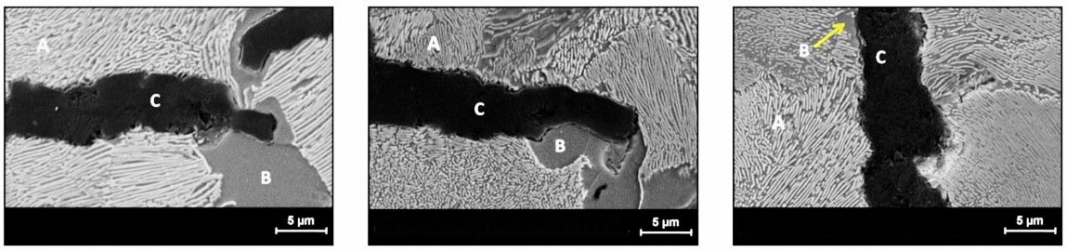


Figure 7
Separation of the Sn film along the boundaries of austenitic grains at a content of Sn: (a) – 0.004%; (b) – 0.021%; (c) – 0.049%

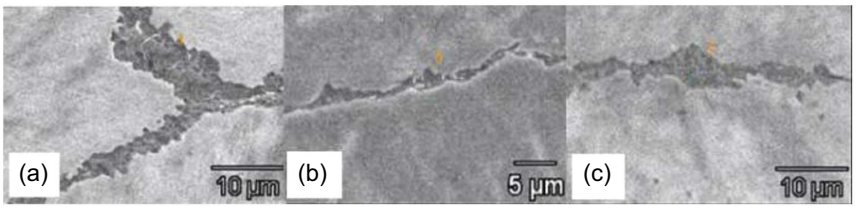
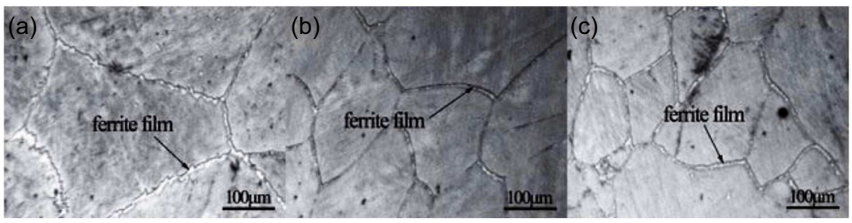


Figure 8
Formation of a ferritic film along the boundaries of austenitic grains at a temperature of 750 °C with a content of Sn: (a) – 0.004%; (b) – 0.021%; (c) – 0.049%



4. Experimental Studies

4.1. Research object

Ductile iron with a structure consisting of 96% pearlite and 4% ferrite was selected as the research object. The iron was treated with a magnesium-cerium master alloy. The chemical composition of the ductile iron (in %) by weight: C = 3.4–3.8; Si = 1.4–1.5; Mn = 0.2–0.5; p = 0.05; S = 0.012; Cr = 0.07; Cu = 0.55–0.65 with tin micro alloying in the amount of Sn = 0.05–0.06%. Experimental specimens in the form of rods 500 mm long and 60 mm in diameter were poured into green, sand-clay molds. Samples for study were cut from the central part of the rod with dimensions of 10 × 10 × 5 mm. The structure of the cast iron was studied in the cast state without heat treatment. Simultaneously, similar samples of ductile iron without tin alloying were cast for comparative evaluation.

4.2. Equipment and methods

Preliminary metallographic studies were conducted on a "LEICA DMIRM" digital optical metallographic microscope using "Image Scope Color M" image analysis software.

For a more detailed assessment of phase transformations and developing pearlite structures, a "FEI SCIOS 2 LOVAC" dual-beam electron microscope with "DUALBEAM" ultra-high-resolution analytical technology was used, enabling the study of the pearlite fine structure in both 2D and 3D projections.

Local chemical microanalysis of the phases was performed using an "EDAX OCTANE ELITE PLUS" X-ray spectral vacuum spectrometer, which utilizes a silicon nitride (Si_3N_4) detector, providing significantly improved sensitivity to the concentration of the elements being determined.

Electron microscopic analysis of pearlite dispersion was performed on a "LEO1455VP" electron microscope.

4.3. Initial cast structure of ductile iron

Figure 9 shows the cast structure of ductile iron, consisting of 96% pearlite and 4% ferrite. The majority of the ferrite was distributed primarily near the nodular graphite inclusions as a decarburized zone.

Figure 9
Cast structure of ductile iron (96% pearlite, 4% ferrite; dark inclusions – graphite)

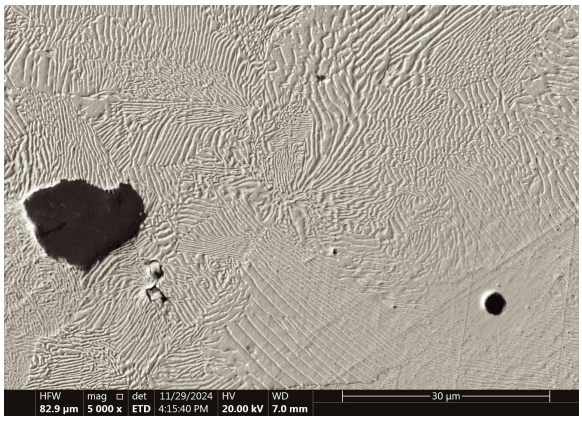


Figure 10 shows the typical distribution of tin intermetallic inclusions in the pearlitic structure of cast iron. The inclusions lack preferred crystallization zones and are randomly distributed both along or near the boundaries of pearlite colonies (austenite grains) and within them. Continuous precipitation of tin intermetallic compounds along the boundaries of pearlite colonies has not been observed. In addition to intermetallic compounds, slag and nonmetallic inclusions of varying morphology are observed in the cast iron structure.

4.4. Study of tin distribution in intermetallic compounds

In a number of works, for example, in Peng et al. [18], and Ribeiro et al. [21], the distribution of tin in cast iron phases was not studied, and the composition of tin intermetallic compounds was not identified.

Figure 10
Typical distribution of intermetallic inclusions in the pearlite structure of ductile iron (indicated by a blue arrow)

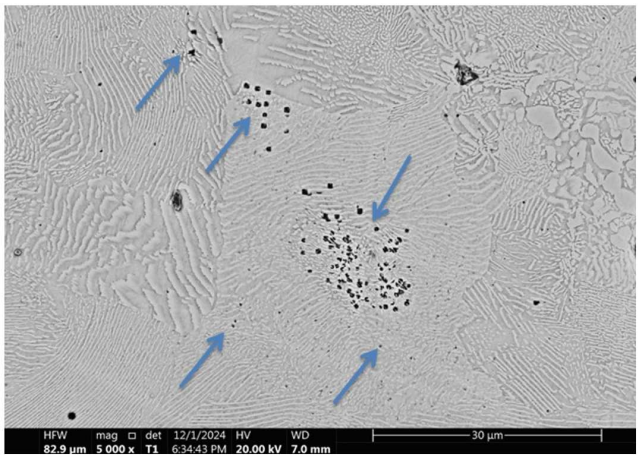


Figure 11 shows the location of the intermetallic compound in the matrix of high-strength cast iron (Figure 11(a)), a discrete linear X-ray spectrum of the intermetallic compound (Figure 11(b)), and chemical composition (Figure 11, Table 1). A complex intermetallic compound with a maximum tin content of 16.14% was recorded in these studies. It should be noted that the intermetallic compound in question (Figure 11(a)) crystallized at the junction of four pearlite colonies (former austenite grains), which does not contradict the scheme in Figure 4.

X-ray analysis (Figure 11(b)) and chemical analysis (Figure 11, Table 1) show that the intermetallic compound under study (Figure 11(a)) is not a homogeneous single crystal but includes in its composition (Figure 11, Table 1) fairly large quantities of iron, copper, and magnesium.

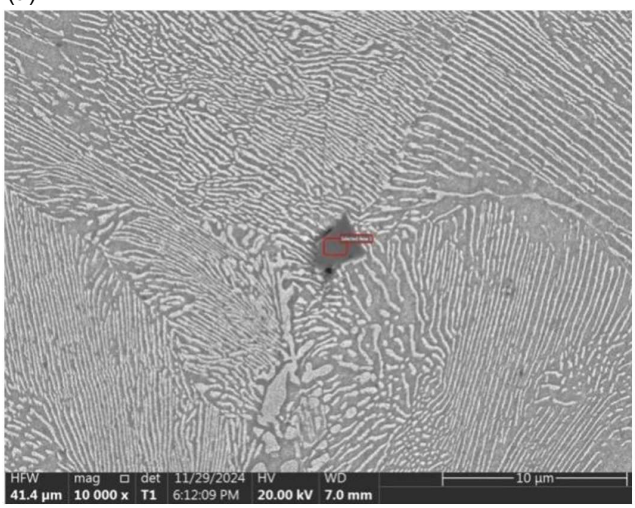
Studies have shown that the tin content in intermetallic compounds of tin-micro alloyed high-strength cast iron varies over a fairly wide range: from 1.5% to 16.0% (see Figure 11).

From the standpoint of alloy theory, this fact can be explained only by the fact that tin intermetallic compounds with its variable content are solid solutions of variable composition based on FeSn, which can be classified as berthollides [23]. A distinctive feature of the berthollide phase is the absence within the homogeneity region of the berthollide-based solid solution of a composition that would correspond to the stoichiometric composition of a specific chemical compound (for example, the FeSn composition). Berthollide phases always have a smooth variable composition (in our studies, a fluctuation from 1.5% Sn to 16.0% Sn was recorded) in a fairly wide homogeneity region. In this case, the actual chemical compound underlying berthollide does not fall within the phase region of homogeneity of the solid solution and lies outside its region [23]. With regard to the Fe–Sn diagram (Figure 2 [15]), the singular point S of the FeSn-based solid solution's homogeneity region can be approximately located at coordinates 607 °C and a concentration of 10.0% Sn, with a homogeneity dome (Figure 2 [15], point S and dotted line) from 1.0 to 20.0% Sn, while the FeSn phase is distinguished along the 68% Sn line (Figure 2 [15]). This hypothesis requires thorough experimental verification, and the final decision lies with X-ray diffraction studies of the intermetallic compound structure.

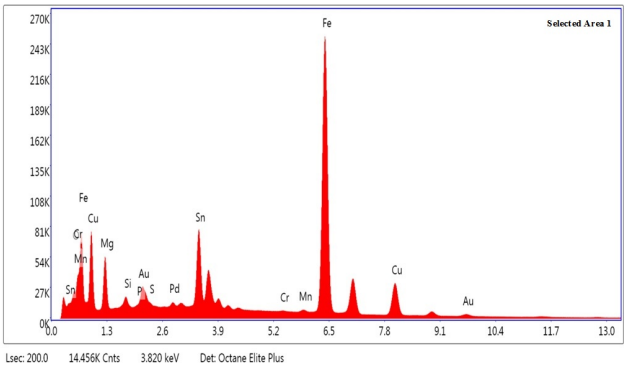
A study of the fine structure of intermetallic compounds indirectly confirms the hypothesis of a FeSn-based solid solution.

Figure 11
Chemical composition of a complex intermetallic compound with a maximum tin content of 16.14%. (a) The location of the intermetallic compound in the cast iron structure. (b) X-ray discrete linear spectrum intermetallic compound

(a)



(b)



As shown above, the crystal structure of the FeSn intermetallic compound is identical to that of graphite; that is, it is layered (Figure 5). Figures 12 and 13 clearly show the layered structure of complex intermetallic compounds with tin, presumably crystals of a solid solution based on layered FeSn as a solvent. It should also be noted that the average size of intermetallic inclusions (Figures 11–13) fluctuates within the range of 200–2000 nm, and in this case, it is appropriate to state the effect of dispersion strengthening of pearlite.

4.5. Study of tin distribution in pearlite lamellar ferrite

The average tin content in pearlite ferrite of the cast iron structure fluctuates significantly: 0.06–0.81% Sn and in some zones up to 1.5% Sn. It should be noted that near the interfaces of pearlite blocks, the tin content in ferrite is usually maximum, but without the formation of a continuous intermetallic layer. At first glance, this contradicts the Fe–Sn diagram, according to which the limiting solubility of Sn in the α-Fe polymorph (ferrite) upon cooling is constant in the range of 1130–765 °C

Table 1
eZAF smart quant results selected area (control intermetallic compounds)

Element	Weight %	Atomic %	Net Int.	Error %	Kratio	*Z*	*A*	*F*
O K	1.23	4.13	436.87	8.18	0.0057	1.2814	0.3742	1.0000
MgK	7.45	16.47	2023.16	8.99	0.0188	1.1936	0.2180	1.0016
SiK	0.87	1.67	454.74	7.97	0.0041	1.1786	0.4125	1.0052
P K	0.22	0.39	114.44	11.20	0.0013	1.1339	0.5281	1.0089
S K	0.28	0.47	170.87	8.24	0.0020	1.1579	0.6384	1.0142
SnL	16.14	7.31	4193.18	1.63	0.1400	0.8534	1.0344	1.0157
CrK	0.14	0.15	61.72	14.54	0.0016	1.0135	0.9398	1.1680
MnK	0.31	0.31	109.06	11.29	0.0031	0.9938	0.9564	1.0644
FeK	60.75	58.46	18384.73	1.83	0.5869	1.0113	0.9685	1.0193
CuK	12.59	10.65	2316.43	2.73	0.1112	0.9755	0.9213	1.0157

Figure 12
Layered structure of intermetallic compounds with tin

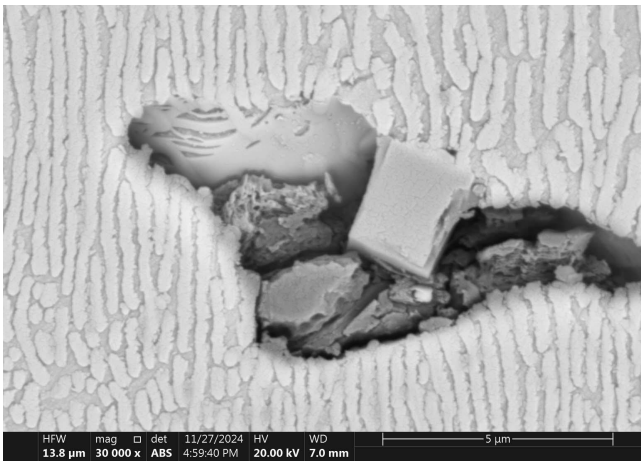
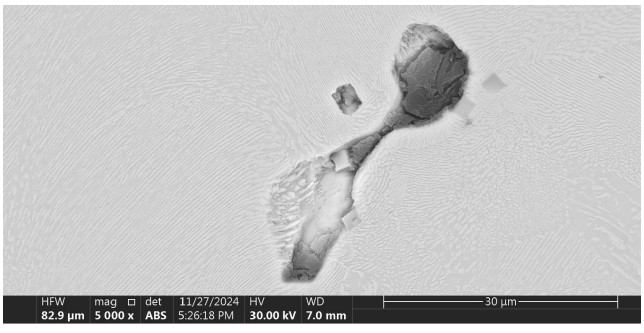


Figure 13
Layered structure of intermetallic compounds with tin precipitated at the junction of several pearlite blocks



(Figure 2 [15]) and is 20.0% by weight. Sn or 10.0% at. Sn on Figure 2 [15] and subsequently decreases to zero below 200 °C (Figure 1 [10]). Consequently, pearlite ferrite in the cast structure of ductile iron is a super-supersaturated (compared to the equilibrium composition according to the Fe–Sn diagram) solid solution of tin in the α-Fe polymorph (ferrite). This phenomenon was discovered in the present study and has not previously been documented in the known literature.

The formation of a super-supersaturated solid solution of ferrite is explained by two factors: first, by nonequilibrium crystallization of the cast iron during modification with spheroidizing master alloys (crystallization supercooling) and accelerated cooling in green sand-clay molds, and second, the leading phase in the eutectoid transformation of austenite is cementite. During crystallization of its plates, closed cells of the cementite framework are formed, filled with ferrite with a super-nonequilibrium concentration of tin. If carbon from the ferrite is used to complete the cementite framework (the phenomenon of decarburization of austenite during its decomposition), then the dissolved tin cannot diffuse outward through the cementite, becoming trapped in the cementite cell and forming a supersaturated solid solution in the ferrite.

This conclusion is well illustrated by the analysis of three intermetallides crystallizing in different zones of the matrix of high-strength cast iron (Figure 14): in pearlite (point 1, Figure 14(a)), in ferrite of pearlite (point 2, Figure 14(a)), and near the interface between two adjacent blocks of pearlite (point 3, Figure 14(a)). Figure 14 contains the location of intermetallides in a matrix of high-strength cast iron (Figure 14(a)), a discrete linear X-ray spectrum of intermetallides (Figure 14(b–d)), and the chemical composition of intermetallides (Figure 14, Tables 2–4).

In the pearlite intermetallic compound (point 1, Figure 14(a)), the tin content is Sn = 5.26% (Figure 14, Table 2); in ferrite intermetallic compound (point 2, Figure 14(a)), Sn = 0.07% (Figure 14, Table 3), and in the intermetallic compound near the interface between two adjacent blocks of pearlite (point 3, Figure 14(a)), Sn = 1.06% (Figure 14, Table 4).

In the performed studies, it was not possible to detect pure intermetallides in accordance with the Fe–Sn diagram (Figure 2 [15]). Chemical analysis of intermetallic inclusions revealed two previously unknown features. First, the tin content in the studied intermetallides Figures 11 and 14, Tables 1–4 varies in a fairly wide range: from 1.5% to 16.0%. Second, the composition of intermetallides includes both spheroidizers of cast iron (Mg and Ce) and its main components (Si, Mn, Cr, Cu, etc.), which have a sufficiently high intensity on radiographs (Figure 11(b) and Figure 14(b–d)). Therefore, the studied intermetallides are complex intermetallides.

This uneven distribution of tin in pearlite colonies is characteristic of virtually the entire cast iron structure and cannot be explained either thermodynamically due to the introduction of tin in microdoses of Sn = 0.05–0.06% (with the exception of intermetallic precipitation, point 1 in Figure 14), or kinetically due to the "heaviness" of tin atoms and their low diffusion mobility. Solute atoms play an important rolae in grain boundary

Table 2
eZAF smart quant results selected area (control intermetallic compounds point 1)

Element	Weight %	Atomic %	Net Int.	Error %	Kratio	*Z*	*A*	*F*
O K	3.24	10.59	1191.85	7.17	0.0163	1.2664	0.4160	1.0000
MgK	0.31	0.68	76.06	13.82	0.0007	1.1792	0.2092	1.0018
SiK	1.66	3.10	840.72	7.28	0.0080	1.1642	0.4307	1.0058
ClK	0.28	0.41	164.86	9.92	0.0022	1.0892	0.7454	1.0263
SnL	5.26	2.32	1303.91	2.44	0.0456	0.8423	1.0485	1.0304
CrK	0.09	0.09	41.24	18.81	0.0011	0.9997	0.9721	1.3416
MnK	0.21	0.20	71.11	13.37	0.0021	0.9800	0.9826	1.0993
FeK	83.56	78.19	23671.92	1.55	0.7907	0.9971	0.9897	1.0071
CuK	5.39	4.43	900.81	3.31	0.0452	0.9610	0.9079	1.0113

Table 3
eZAF smart quant results selected area (control intermetallic compounds point 2)

Element	Weight %	Atomic %	Net Int.	Error %	Kratio	*Z*	*A*	*F*
MgK	0.51	1.15	133.46	11.46	0.0013	1.1786	0.2122	1.0020
SiK	1.73	3.34	928.31	7.21	0.0085	1.1635	0.4337	1.0066
P K	0.22	0.39	114.65	10.89	0.0013	1.1192	0.5464	1.0113
S K	0.71	1.20	440.49	5.67	0.0053	1.1427	0.6567	1.0181
SnL	0.07	0.03	19.57	43.13	0.0007	0.8415	1.0497	1.0388
CaK	0.13	0.17	72.69	10.24	0.0014	1.1071	0.9110	1.1043
TiK	2.71	3.07	1545.78	3.04	0.0308	1.0061	0.9605	1.2117
CeL	0.62	0.24	117.19	11.74	0.0058	0.8066	1.0850	1.1047
MnK	0.21	0.20	75.32	13.17	0.0021	0.9789	0.9873	1.1130
FeK	92.32	89.59	27520.68	1.48	0.8864	0.9958	0.9934	1.0012
CuK	0.50	0.42	87.07	11.80	0.0042	0.9595	0.9005	1.0105
AsK	0.28	0.20	19.63	36.53	0.0024	0.9008	0.9601	1.0409

Table 4
eZAF smart quant results selected area (control intermetallic compounds point 3)

Element	Weight %	Atomic %	Net Int.	Error %	Kratio	*Z*	*A*	*F*
O K	3.86	12.14	1517.99	7.02	0.0199	1.2558	0.4279	1.0000
MgK	0.43	0.89	108.32	12.86	0.0010	1.1691	0.2100	1.0020
SiK	1.59	2.85	840.99	7.23	0.0077	1.1541	0.4328	1.0065
S K	0.32	0.51	197.68	7.25	0.0024	1.1333	0.6581	1.0182
ClK	0.20	0.28	121.43	10.95	0.0016	1.0795	0.7467	1.0294
SnL	1.06	0.45	276.64	5.17	0.0093	0.8346	1.0514	1.0380
CrK	0.12	0.12	64.20	15.12	0.0016	0.9903	0.9843	1.4591
MnK	0.31	0.29	115.03	10.53	0.0033	0.9706	0.9923	1.1270
FeK	87.27	78.65	25849.66	1.47	0.8314	0.9874	0.9975	1.0058
CuK	4.84	3.83	839.43	3.32	0.0406	0.9512	0.9078	1.0099

migration phenomena, which are crucial for understanding the microstructural evolution of metals.

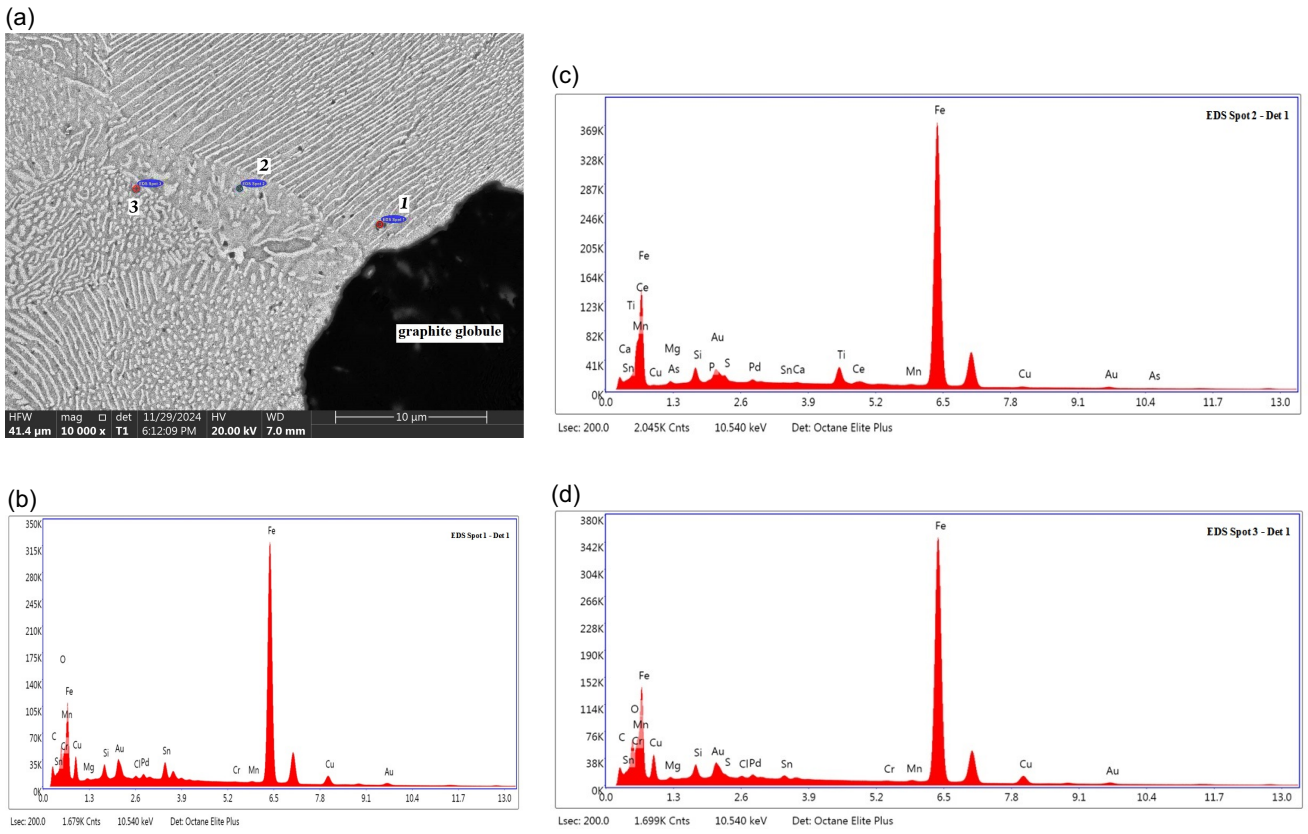
For example, in Mavrikakis et al. [24, 25] and Dumont et al. [26], Sn segregation at migrating boundaries during recrystallization in a Fe–Si–Sn ferritic alloy was studied using atomic probe tomography. Experimental data revealed the presence of a solute depletion zone ahead of the moving interface. The behavior of Sn was explained by the solute drag theory.

A difference in segregation between the two studied migrating interfaces was discovered, which can be explained by changes in either the binding energy or the intrinsic velocity of each interface. These conclusions may be valid for the eutectoid decomposition of austenite in the solid state, but the answer must be sought in the processes of primary crystallization of the melt.

This uneven tin distribution can be explained by spinodal decomposition of the liquid phase ahead of the austenite crystallization front in the solid–liquid region. In Guo et al. [27] and Guin et al. [28], the process of spinodal decomposition near moving grain boundaries was studied using a phase-field model. Modeling results show that the pattern directed toward the grain boundaries is anisotropic, and with increasing atomic mobility within the grain boundaries, the pattern of the crystallizing phase changes from parallel to the original grain boundary to perpendicular. This phenomenon is well illustrated by the structure of pearlite colonies in Figure 14.

Figure 14

Chemical composition and tin content: in the complex intermetallic compound (point 1: Sn = 5.26%), in ferrite inside the pearlite colony (point 2: Sn = 0.07%), and near the interface between two adjacent pearlite cells (point 3: Sn = 1.06%). (a) The location of the intermetallic compound point 1, point 2, and point 3 in the cast iron structure. (b) X-ray discrete linear spectrum intermetallic compound point 1. (c) X-ray discrete linear spectrum intermetallic compound point 2. (d) X-ray discrete linear spectrum intermetallic compound point 3



During the initial period of austenite crystallization from the melt, a volume of melt with an increased tin content is formed at the austenite grain-melt phase boundary. For example, an austenite grain (point 1, Figure 14) is a primarily crystallizing grain, in front of which a supersaturated microzone of liquid melt is formed (future grains, points 2 and 3, Figure 14). Tin is "squeezed" into this liquid microzone by similarly growing neighboring primary austenite grains. As soon as the tin concentration in this liquid microzone reaches a supercritical level, it will spontaneously stratify by the spinodal decomposition mechanism [25, 26] near the moving interphase boundaries into two regions with a low tin concentration (point 2, Figure 14(a)) high tin concentration (point 3, Figure 14). Moreover, the crystallization of the two resulting regions will proceed through different mechanisms, as evidenced by the pronounced anisotropy of the texture of the adjacent pearlite colonies.

While the different tin contents in the structures of cast iron and steel can be formally explained using established metallographic paradigms, the precise identification of the tin intermetallics themselves in the Fe–Sn diagram still requires further research.

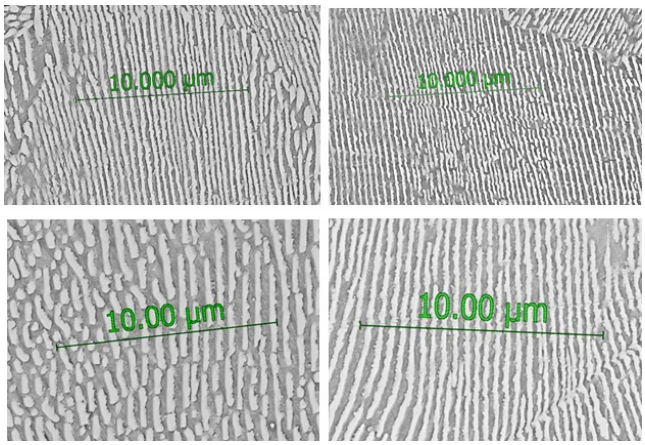
In a recent study of Shen et al. [14], the thermodynamic and topological properties of intermetallics in the Fe–Sn system were investigated using experimental data, (ab initio) calculations, and the Calphad phase diagram method. Based on the results obtained, the metastable Fe_3Sn phase was introduced into the diagram, and the phase positions of Fe_5Sn_3 and Fe_3Sn_2 were refined in newly measured, adjusted temperature ranges.

It is also worth noting the data of the work of Park et al. [10], in which experimental studies and repeated optimization of the parameters of the Fe–Sn diagram were carried out with an emphasis on refining the shape of the immiscibility regions. Park et al. [10] used three different experimental methods: differential scanning calorimetry, electromagnetic levitation, and contact angle measurement. The proposed thermodynamic model of the Fe–Sn diagram has a higher accuracy in predicting the solubility of tin in the body-centered cubic structure compared to previous estimates. This is achieved by re-evaluating the Gibbs energies of the FeSn and $FeSn_2$ compounds and the peritectic reaction associated with Fe_5Sn_3.

4.6. Determination of pearlite dispersion

Pearlite dispersion was determined by a direct method. The number of cementite plates intersected by its ***n*** was counted on an arbitrary secant line 10 μm long. The average distance between cementite plates (in μm) was calculated using the formula: = 10/2*n*. Examples of interlamellar distance measurements in pearlite are shown in Figure 15. The degree of pearlite dispersion was determined for high-strength cast iron both after

Figure 15
Examples of determining the degree of dispersion of pearlite, ×10000



its microalloying with tin in an amount of Sn = 0.05–0.06% and without alloying. The results were unexpected and impressive. The average degree of pearlite dispersion in both cast irons was practically the same. In cast iron with tin, Δ_{Sn} = 0.13 µm, while in cast iron without tin, Δ_0 = 0.14 µm. Thus, based on experimental data in cast irons with and without tin, there is no difference in the interlamellar distance in pearlite between ferrite and cementite; that is, the degree of dispersion of pearlite does not depend on its alloying with tin.

The obtained data are confirmed by the conclusions of the work of Shen et al. [14], which experimentally established the absence of a significant effect of tin on the eutectic transformation temperature.

It has also been shown in Gumienny et al. [29] that tin narrows the temperature range of the austenitic transformation, which may indirectly be a partial change in the dispersion of pearlite.

At the same time, the obtained data provide a consistent explanation for the characteristic changes in the properties of cast iron and steel without invoking the universal principle of "changes in pearlite dispersion". The key factor here is the formation of a supersaturated solid solution of ferrite within the closed lamellar framework of pearlite cementite. This explains the increase in hardness due to the overstressed state of ferrite and the distortion of its lattice by dissolved heavy and giant tin atoms. The increased corrosion resistance of the alloy is explained by the high degree of tin alloying of the ferrite, as well as by the fact that the surface layer of pearlite blocks is supersaturated with tin (the barrier layer) without the formation of continuous films [3–5]. High antifriction and wear-resistant properties are enhanced again by the highly alloyed ferrite of pearlite (Figure 14), as well as by the presence of layered inclusions of intermetallic compounds (Figures 12 and 13), which function as supporting hard micropoints in the contacting tribosurfaces. In addition, micropores in the volume of intermetallic inclusions (Figures 12 and 13) act as containers for collecting wear products, which further increases the wear resistance of the surface.

Based on the research conducted, the following conclusions can be drawn.

5. Conclusion

1) Based on an analysis of literary sources, it has been established that during the cooling of iron–carbon alloys with a high Sn content (0.10–0.15% or more), Sn dissolved in austenite diffuses to the interphase surfaces of austenite grains during the eutectoid phase transformation, forming a barrier layer supersaturated with tin, which impedes the diffusion of carbon from the austenite.
2) The barrier layer supersaturated with tin disintegrates during cooling, precipitating intermetallic compounds and a ferrite film, which are the main cause of embrittlement of the cast iron's metallic base and increased hardness.
3) Supersaturation of austenite "preserved" with tin will lead to its dispersion strengthening during the eutectoid transformation due to the precipitation of nanometer-sized intermetallic compounds, which further strengthens pearlite.
4) The Sn content in the studied intermetallics varies over a fairly wide range: from 1.5% to 16.0%. From the standpoint of alloy theory, this fact can be explained only by the fact that tin intermetallic compounds with their variable content that are solid homogeneous solutions based on FeSn.
5) An assessment of tin distribution in pearlite ferrite plates was performed for the first time and also revealed previously unknown effects. The average tin content in pearlite ferrite of the cast iron structure varies significantly: 0.060.81% Sn and in some zones up to 1.5% Sn. Consequently, pearlite ferrite in the cast structure of ductile iron is a supersaturated (compared to the equilibrium composition according to the Fe–Sn diagram) solid solution of tin in the α-Fe polymorph (ferrite).
6) The degree of pearlite dispersion was determined in ductile iron both after its microalloying with tin at a concentration of Sn = 0.05–0.06% and without alloying. The results were unexpected and impressive. The average degree of pearlite dispersion in both cast irons was virtually identical. In the cast iron with tin, Δ_{Sn} = 0.13 µm, while in the cast iron without tin, $_0$= 0.14 µm. Thus, based on the experimental data for cast irons with and without tin, there is no difference in the interlamellar spacing in pearlite between ferrite and cementite; that is, the degree of pearlite dispersion is independent of its alloying with tin.
7) The conducted studies reliably demonstrate the feasibility of Sn microalloying both from the standpoint of effectively managing the microstructure of iron–carbon alloys and from the standpoint of reducing the environmental impact of iron and steel production processes.

Ethical Statement

This study does not contain any studies with human or animal subjects performed by the author.

Conflicts of Interest

The author declares that he has no conflicts of interest to this work.

Data Availability Statement

Data sharing is not applicable to this article as no new data were created or analyzed in this study.

Author Contribution Statement

Sergey Vasilyevich Davydov: Conceptualization, Software, Methodology, Validation, Formal analysis, Investigation, Resources, Data curation, Writing – original draft, Writing – review & editing, Visualization, Supervision, Project administration.

References

[1] Mishra, H. S., Sahu, R., & Padan, D. S. (2024). Effect of Sn alloying on the microstructural features and mechanical properties of gray cast iron. *Journal of Materials Engineering and Performance*, *33*(22), 12494–12502. https://doi.org/10.1007/s11665-023-08834-0

[2] Mishra, H. S., Sahu, R., & Padan, D. S. (2021). Effect of tin as alloying element on grey iron automobile casting. In *Recent advances in manufacturing processes: Select proceedings of RDMPMC 2020*, 141–152. https://doi.org/10.1007/978-981-16-3686-8_12

[3] Shin, W. S., Baek, S., & Kim, Y. J. (2022). Effect of Sn addition on the microstructure and friction–wear properties of a nodular graphite cast iron. *Korean Journal of Metals and Materials*, *60*(6), 471–477. https://doi.org/10.3365/KJMM.2022.60.6.471

[4] Li, Q., Zhang, Y., Zhang, Y., Liu, H., Ren, H., Zhong, Y., . . . , & Huang, W. (2020). Influence of Sn and Nb additions on the microstructure and wear characteristics of a gray cast iron. *Applied Physics A*, *126*(4), 282. https://doi.org/10.1007/S00339-020-03468-8

[5] Li, Y., Chen, R., Wang, Q., Cao, W., Wang, X., Xia, Y., ..., & Li, G. (2022). Effect of V and Sn on microstructure and mechanical properties of gray cast iron. *China Foundry*, *19*(5), 427–434. https://doi.org/10.1007/s41230-022-2001-6

[6] Zhang, Y., & Han, J. (2019). Studying the machinability of tin-bearing free-cutting steel. *Inorganic Materials: Applied Research*, *10*(3), 726–729. https://doi.org/10.1134/S2075113319030420

[7] Pandey, S., Mishra, K. K., Ghosh, P., Singh, A. K., & Jha, S. K. (2023). Characterization of tin-plated steel. *Frontiers in Materials*, *10*, 1113438. https://doi.org/10.3389/fmats.2023.1113438

[8] Glebovsky, V. (2021). Electromagnetic levitation of metal melts. In D. R. Sahu & V. N. Stavrou (Eds.), *Magnetic materials and magnetic levitation* (pp. 1–30). IntechOpen. https://doi.org/10.5772/intechopen.92230

[9] Buonincontri, M. (2020). *Electrolytic removal of tin from tinplated scraps*. [Master's thesis, Politecnico di Milano]. POLITesi. https://hdl.handle.net/10589/179197

[10] Park, W. B., Bernhard, M., Presoly, P., & Kang, Y. B. (2023). Thermodynamic modeling of the Fe–Sn system including an experimental re-assessment of the liquid miscibility gap. *Journal of Materials Informatics*, *3*(1), 5. https://doi.org/10.20517/jmi.2022.37

[11] Hari Kumar, K. C., Wollants, P., & Delaey, L. (1996). Thermodynamic evaluation of Fe–Sn phase diagram. *Calphad*, *20*(2), 139–149. https://doi.org/10.1016/S0364-5916(96)00021-1

[12] Lacaze, J., & Sertucha, J. (2017). Effect of tin on the phase transformations of cast irons. *Journal of Phase Equilibria and Diffusion*, *38*(5), 743–749. https://doi.org/10.1007/s11669-017-0561-8

[13] Maruyama, N., & Ban-ya, S. (1980). Ryūdōhō ni yoru Fe-Cu, Fe-Cr oyobi Fe-Sn-kei gōkin no katsuryō sokutei [Measurement of activities in liquid Fe-Cu, Fe-Cr and Fe-Sn alloys by a transportation method]. *Journal of the Japan Institute of Metals and Materials, 44*(12), 1422–1431. https://doi.org/10.2320/jinstmet1952.44.12_1422

[14] Shen, C., Samathrakis, I., Hu, K., Singh, H. K., Fortunato, N., Liu, H., . . . , & Zhang, H. (2022). Thermodynamical and topological properties of metastable Fe_3Sn. *npj Computational Materials*, *8*(1), 248. https://doi.org/10.1038/s41524-022-00917-1

[15] Lyakishev, N. P. (Ed.). (2001). *Diagrammy sostoyaniya dvoynykh metallicheskikh sistem* [Diagrams of the state of double metal systems]. Машиностроение.

[16] Bannykh, O. A., Budberg, P. B., & Alisova, S. P. (1986). *Diagrammy sostoyaniya dvoynykh i mnogokomponentnykh sistem na osnove zheleza* [Diagrams of the state of binary and multicomponent systems based on iron]. Металлургия.

[17] von Goldbeck, O. K. (1982). *Iron—Binary phase diagrams*. Springer. https://doi.org/10.1007/978-3-662-08024-5

[18] Peng, H., Chen, W., Chen, L., & Guo, D. (2014). Effect of tin on hot ductility and high-temperature oxidation behavior of 20CrMnTi steel. *High Temperature Materials and Processes*, *33*(2), 179–185. https://doi.org/10.1515/htmp-2013-0028

[19] Patnaik, P. (2003). *Handbook of inorganic chemicals*. McGraw-Hill.

[20] Sun, G., & Tao, S. (2018). Duplex heterogeneous nucleation behavior of precipitates in C–Mn steel containing Sn. *Metallurgical and Materials Transactions B*, *49*(2), 519–523. https://doi.org/10.1007/s11663-018-1180-4

[21] Ribeiro, B. C. M., Rocha, F. M., Andrade, B. M., Lopes, W., & Corrêa, E. C. S. (2020). Influence of different concentrations of silicon, copper and tin in the microstructure and in the mechanical properties of compacted graphite iron. *Materials Research*, *23*(2), e20190678. https://doi.org/10.1590/1980-5373-mr-2019-0678

[22] Walter, C., Menezes, P. W., & Driess, M. (2021). Perspective on intermetallics towards efficient electrocatalytic water-splitting. *Chemical Science*, *12*(25), 8603–8631. https://doi.org/10.1039/D1SC01901E

[23] Davydov, S. V. (2020). Low-temperature carbide transformation in pearlite of medium-carbon steels. *Steel in Translation*, *50*(9), 639–647. https://doi.org/10.3103/S0967091220090041

[24] Mavrikakis, N., Saikaly, W., Mangelinck, D., & Dumont, M. (2020). Segregation of Sn on migrating interfaces of ferrite recrystallisation: Quantification through APT measurements and comparison with the solute drag theory. *Materialia*, *9*, 100541. https://doi.org/10.1016/j.mtla.2019.100541

[25] Mavrikakis, N., Saikaly, W., Calvillo, P. R., Campos, A. P. C., Jacomet, S., Bozzolo, N., . . . , & Dumont, M. (2022). How Sn addition influences texture development in single-phase Fe alloys: Correlation between local chemical information, microstructure and recrystallisation. *Materials Characterization*, *190*, 112072. https://doi.org/10.1016/j.matchar.2022.112072

[26] Dumont, M., Mavrikakis, N., Saikaly, W., & Mangelinck, D. (2023). Kinetics of static recrystallization in Sn-added Fe-Si alloys. *Metallurgical Research & Technology*, *120*(5), 509. https://doi.org/10.1051/metal/2023067

[27] Guo, C., Gao, Y., Cui, Y., Zhao, Y., Xu, C., Sui, S., ..., & Zhang, Z. (2023). Phase-field simulation of the spinodal

decomposition process near moving grain boundaries. *Materials Today Communications*, *35*, 105811. https://doi.org/10.1016/j.mtcomm.2023.105811

[28] Guin, S., Verma, M., Bandyopadhyay, S., Lo, Y.-C., & Mukherjee, R. (2024). Solute segregation in a moving grain boundary: A phase-field approach. *Modelling and Simulation in Materials Science and Engineering, 32*(6), 065009. https://doi.org/10.1088/1361-651X/ad585d

[29] Gumienny, G., Kurowska, B., & Fabian, P. (2020). Compacted graphite iron with the addition of tin. *Archives of Foundry Engineering*, *20*(3), 15–20. https://doi.org/10.24425/afe.2020.133323

How to Cite: Davydov, S. V. (2026). Crystallization of Tin in Iron–Carbon Alloys. *Archives of Advanced Engineering Science*, *4*(4), 390–401. https://doi.org/10.47852/bonviewAAES62028822